ADAPTIVE EAGLE DYNAMIC SOLUTION ADAPTATION AND GRID QUALITY ENHANCEMENT

Phu Vinh Luong
Naval Oceanographic Office
Stennis Space Center, MS 39529

J. F. Thompson, B. Gatlin, C. W. Mastin, H. J. Kim
NSF Engineering Research Center for Computational Field Simulation
Mississippi State University
Mississippi State, MS 39762

ABSTRACT

In the effort described here, the elliptic grid generation procedure in the EAGLE grid code has been separated from the main code into a subroutine, and a new subroutine which evaluates several grid quality measures at each grid point has been added. The elliptic grid routine can now be called, either by a CFD code to generate a new adaptive grid based on flow variables and quality measures through multiple adaptation, or by the EAGLE main code to generate a grid based on quality measure variables through static adaptation. Arrays of flow variables can be read into the EAGLE grid code for use in static adaptation as well. These major changes in the EAGLE adaptive grid system make it easier to convert any CFD code that operates on a block–structured grid (or single–block grid) into a multiple adaptive code.

INTRODUCTION

The requirements of accuracy and efficiency for obtaining solutions to PDE's have always been a conflict in numerical methods for solving field problems. On the one hand, it is well known that increasing the number of grid points implies decreasing the local truncation error. This, however, results in long computation time due to large numbers of grid points. On the other hand, shorter computation time can be achieved by decreasing the number of grid points, but the result is a less accurate solution.

Adaptive grid generation techniques are a means for resolving this conflict. For many practical problems, the initial grid may not be the best suited for a particular physical problem. For example, the location of flow features, such as shocks, boundary and shear layers, and wake regions, are not known before the grid is generated. In multiple adaptive grid generation, grid points are moved continually to respond to these features in the flow field as they develop. This adaptation can reduce the oscillations associated with inadequate resolution of large gradients, allowing sharper shocks and better representation of boundary layers. Thus it is possible to achieve both efficiency and high accuracy for numerical solutions of PDE's. Several basic techniques involved in adaptive grid generation are discussed in Ref. (1).

In the earlier form of the adaptive EAGLE system (2, 3), the coupling of the adaptive grid system with a CFD code required the encapsulation of both the entire grid code and the CFD flow code into separate subroutines, and the construction of a driver to call each. This was inefficient that it included some unnecessary parts of the grid code and required significant modification, and perhaps restructuring, of the CFD code. In particular, the flow code arrays and/or the grid code arrays had to be modified to be compatible in structure.

The conversion procedure is accomplished by adding the elliptic grid generation subroutine, and certain other subroutines from the EAGLE grid system that are involved in the elliptic grid generation process, to the flow code. The CFD code may then call the elliptic grid generation routine at each time step when a new grid is desired. The CFD code passes its current solution to this EAGLE routine via a scratch file. This structure eliminates the need for compatibility between CFD and grid arrays. One restrictions is that the initial grid must be generated by the EAGLE system, or be processed through that system. This provides the necessary parameters and structural information to be read from files by the adaptive EAGLE routine.

In the present work, the control function approach is used as the basic mechanism for the adaptive grid generation. The static and multiple adaptive grid generation techniques are investigated by formulating the control functions in terms of either grid quality measures, the flow solution, or both.

Previous work (2, 3) with the adaptive EAGLE system allowed the grid to only adapt to the gradient of a variable. The work described here has extended this adaptive mechanism to also allow adaptation to the curvature of a variable or to the variable itself. The system provides for different weight functions in each coordinate direction. In addition, the mechanism now includes the ability to calculate the weight functions as weighted averages of weight functions from several flow variables and/or quality measures. This allows the adaptation to take into account the effect of many of the flow variables instead of just one. The construction of the weighted average of flow variables and quality measures, and the choice of adaptation to gradient, curvature, or variable, are all controlled in each coordinate directions through input parameters. The quality measures now available in the EAGLE grid system are skewness, aspect ratio, arc length, and smoothness of the grid. These grid quality measures, and the resulting control and weight function values, can be output for graphical contouring.

ADAPTIVE MECHANISM

Control Function Approach

The control function approach to adaptation is developed by noting the correspondence between the 1D form of the system,

$$x_{\xi\xi} + Px_\xi = 0 \qquad (1)$$

and the differential form of the equidistribution principle, Wx_ξ = constant,

$$Wx_{\xi\xi} + W_\xi x_\xi = 0 \qquad (2)$$

where P is the function to control the coordinate line spacing, and W is the weight function.

From (1) and (2) the control function can be defined in terms of the weight function and its derivative as

$$P = \frac{W_\xi}{W} \tag{3}$$

This equation can be extended in a general 3D form as

$$P_i = \frac{W_{\xi^i}}{W} \tag{4}$$

This approach was suggested by Anderson (Ref. 4, 5), and has been applied with success for 2D configurations by Johnson and Thompson (Ref. 6) and for 3D configurations by Kim and Thompson (Ref. 2) and by Tu and Thompson (Ref. 3).

The complete generalization of (4) was proposed by Eiseman (Ref. 7) as

$$P_i = \sum_{j=1}^{3} \frac{g^{ij}}{g^{ii}} \frac{(W_j)_{\xi^j}}{W_i} \tag{5}$$

where W_i is the weight function chosen for the ξ^i direction. This definition of the control functions provides a convenient means to specify three separate control functions, with one in each coordinate direction.

In order to preserve the geometrical characteristics of the existing grid, it is practical to construct the control functions in such a manner that the control functions defined by (5) are added to the initial set of control functions obtained from the geometry, i.e.,

$$\bar{P}_i = (P_i)_g + C_i(P_i)_w \qquad i = 1,2,3 \tag{6}$$

where

$(P_i)_g$: control function based on geometry

$(P_i)_w$: control function based on weight function

In these equations the weight function W can be computed by different formulas for different adaptive mechanisms:

Adaptation to

$$\begin{aligned} &\textit{Variable} && : \quad W = 1 + |V| \\ &\textit{Gradient} && : \quad W = 1 + |\nabla V| \\ &\textit{Curvature} && : \quad W = (1 + \beta\,|K|)\sqrt{1 + \alpha\,|\nabla V|^2} \end{aligned} \tag{7}$$

where V can be either a flow solution variable or a grid quality measure. Here α and β are on the range 0−1, and

$$K = \frac{\nabla^2 V}{(1 + |\nabla V|^2)^{3/2}} \tag{8}$$

is the curvature of the variable V.

Using these definitions of the control functions, the elliptic generation system becomes an adaptive grid generation system. This system is then solved iteratively in adaptive EAGLE by the point SOR method to generate the adaptive grid.

Grid Quality Measures

The objective of this part of the investigation was to develop a means of evaluating grids through the computation of certain grid properties that are related to grid quality and to develop techniques for estimating the truncation error. Following Kerlick and Klopfer (Ref. 8), and Gatlin, et. al. (Ref. 9), the grid quality measures are taken as skew angle, aspect ratio, grid Laplacian, and arc length. Techniques for estimating the truncation error due to the work of Mastin (Ref. 10) are also included. At each grid point in a general 3D grid, each property can have three values associated with the three directions. The approach taken in this investigation is to treat each surface of constant ξ^i separately for ease in graphical interpretation.

skew angle

The minimum skew angle between intersecting grid lines is one of the most important measurable grid properties. This angle can be expressed in terms of the covariant metric elements as

$$\theta_{ij} = \cos^{-1}\left\{\frac{g_{ij}}{\sqrt{g_{ii}g_{jj}}}\right\} \tag{9}$$

Since $g_{12} = g_{21}$, $g_{13} = g_{31}$ and $g_{23} = g_{32}$, the three skew angles associated with each grid point in a 3D grid are θ_{12}, θ_{23} and θ_{31}.

aspect ratio

Since aspect ratio is the ratio of the length of the sides of a grid cell, it can be defined in two different ways. For example, on a surface of constant ξ^k, this ratio can be expressed in terms of metric elements g_{ii} and g_{jj} as

$$AR_{ij} = \sqrt{\frac{g_{ii}}{g_{jj}}} \tag{10a}$$

or

$$AR_{ji} = \sqrt{\frac{g_{jj}}{g_{ii}}} \tag{10b}$$

Large changes in aspect ratio of grids from one part of the field to another may inhibit the convergence of viscous flow solutions to a steady state.

Laplacian

A useful measure of the smoothness of a grid is the Laplacian of the curvilinear system, $\nabla^2\xi^i$, $i = 1,2,3$, which is simply the rate of change of grid point density in the grid. For a perfectly uniform grid, the grid Laplacian would vanish everywhere, but exceedingly large values may arise in highly stretched grids. The mathematical representation of the grid Laplacian is defined in terms of the contravariant metric elements g^{ij}, the contravariant base vectors a^i and the position vector r as

$$\nabla^2\xi^\ell = -\sum_{i=1}^{3}\sum_{j=1}^{3} g^{ij}\, a^\ell \cdot r_{\xi^i\xi^j} \qquad \ell = 1,2,3 \tag{11}$$

arc length

Another important measure of the grid quality is the local rate at which grid spacing changes. On a coordinate surface of constant ξ^3, and along a coordinate line of constant ξ^2, the grid spacing can be defined as

$$d_i = [(x_{i+1} - x_i)^2 + (y_{i+1} - y_i)^2 + (z_{i+1} - z_i)^2]^{\frac{1}{2}} \quad (12a)$$

The normalized rate at which grid spacing changes (ARCL) is then

$$(ARCL)_i = \frac{d_i - d_{i-1}}{\frac{1}{2}(d_i + d_{i-1})} \quad (12b)$$

error estimations

The objective of this section is to present heuristic error estimates which give order of magnitude approximations for the truncation error and the solution error in the numerical solution of the Euler equations for compressible flow and other systems of conservation laws. Any conservation law can be written in a general form as

$$u_t + f_x + g_y + h_z = 0 \quad (13a)$$

The transformation of this system to an arbitrary curvilinear coordinate system is

$$U_t + F_{\xi^1} + G_{\xi^2} + H_{\xi^3} = 0 \quad (13b)$$

where $\sqrt{g}$ is the Jacobian of the transformation and

$$F = \sqrt{g}\,(\xi^1_x f + \xi^1_y g + \xi^1_z h)$$

$$G = \sqrt{g}\,(\xi^2_x f + \xi^2_y g + \xi^2_z h)$$

Let h be the spacing of the fine grid, and nh be the spacing of the coarse grid. Let L_h be the difference approximation operator on the fine grid, and L_{nh} be the difference approximation operator on the coarse grid. Then the finite difference approximation of the PDE can be represented on the fine grid as

$$u_t + f_x + g_y + h_z = L_h(F,G,H) + T(h)^p \quad (13c)$$

and on the coarse grid as

$$u_t + f_x + g_y + h_z = L_{nh}(F,G,H) + T(nh)^p \quad (13d)$$

where n is an integer.

From (13c) and (13d), the estimate of the truncation error on the fine grid can be computed as

$$T(h)^p = \frac{L_{nh} - L_h}{(1 - n^p)} \quad (14)$$

A similar procedure can be used to compute the error in the numerical solution. Such a procedure has long been used in the numerical solution of ordinary differential equations and is referred to as Richardson extrapolation. Even though numerical solutions must be computed on both fine and coarse grids, the error estimates which result do not have the large peaks at solution singularities which can be encountered with the truncation error computed from difference approximation of higher derivatives. Thus the solution error estimates may sometimes be more useful in the construction of adaptive grids.

Assume that there are two numerical solutions of order p accuracy for (13b) that have been computed on a fine grid and on a coarse grid, with grid spacing h and nh, respectively, in each coordinate direction. Assuming that the same pth order method is used in both cases, then the relation between the two numerical solutions and the actual solution u of the PDE can be established as

$$u = U_h + R(h)^p \quad (15a)$$

and

$$u = U_{nh} + R(nh)^p \quad (15b)$$

From these equations, an extrapolated value of u can be computed as

$$u = \frac{n^p U_h - U_{nh}}{(n^p - 1)} \quad (15c)$$

Thus the estimate of the error in the numerical solution computed on the h grid is:

$$u - U_h = \frac{U_h - U_{nh}}{(n^p - 1)} \quad (15d)$$

RESULTS AND DISCUSSION

The adaptive grid generation system based on the control function approach as described in the previous chapters has been used to generate static and multiple adaptive grids for several geometries (Ref. 11). Some of these results are presented in this section. The static adaptive grids were obtained by adapting the initial grids to either grid quality measure variables or to existing flow solution variables. The multiple adaptive procedure was tested on several different configurations with the adaptive MISSE Euler flow code (Ref. 12) for transonic and supersonic flow cases, and with the adaptive INS3D flow code (Ref. 13) for incompressible flow.

Adaptation to Quality Measures

Some examples of the grid quality adaptation are shown in Figure 1 for adaptation to various quality measures. (In Ref. 11, color contour plots of the quality measures and the other adaptive features are given.) Figures 2a–d shows the difference of the average skew angle between the initial and adaptive grids. The same number of total adaptive iterations were run in each case. The control functions were updated based on the geometry of the previous grid, rather than the initial grid, at each adaptation.

Comparison of Figure 1b with Figure 1a shows that adaptation to the skewness is effective in reducing the skewness in one region, while increasing the skewness in other regions of the grid. A small improvement in aspect ratio occurs, but the smoothness of the grid is decreased.

Comparison of Figure 1c with Figure 1a indicates that adaptation to aspect ratio does improve both aspect ratio and smoothness of the grid; the skewness is increased, however. Comparison of Figure 1d with Figure 1a shows that adaptation to smoothness improves the skewness and aspect ratio of the grid effectively, but the adaptive grid is not as smooth as the initial elliptic grid.

Figure 1e shows the beneficial effect of including adaptation to aspect ratio, arc length, and smoothness, with adaptation to skewness: the skewness is reduced more by the combination than with skewness adaptation alone. A little improvement occurs in aspect ratio; the smoothness of the grid does, however, decrease.

Results from these examples show that the adaptation to the combination of all grid quality measures, or to each individually, can improve some grid properties while damaging others. For example the adaptation to the Laplacian of this particular grid can reduce the skewness, but the resulting adaptive grid is not as smooth as the initial grid. The choice of the adaptive variable for the adaptation very much depends on what property of the grid needs to be improved and the configurations of the grids.

Multiple Adaptation

Results of multiple adaptation performed with the adaptive MISSE Euler flow code are shown in Figures 3–8. In all these plots, NIT is the total number of time steps, INT indicates the number of time steps at which the first adaptation is performed, NCL is the number of time steps between each adaptation, and MAXINT indicates the number of time steps at which the last adaptation is performed. Values of weight functions (AWT_1, AWT_2), weight coefficients (C_1, C_2), adaptive variables density (RHO_1, RHO_2), pressure ($PRES_1$, $PRES_2$) are given for the ξ^1 and the ξ^2 directions, respectively. For example, $AWT = GRAD, CURV, C_1 = 0.5, C_2 = 0.3, RHO = 1,0, PRES = 0,1$ and $\alpha = 1, \beta = 1$, can be interpreted as adaptation to the density gradient in the ξ^1 direction with $C_1 = 0.5$, and to the curvature of the pressure in the ξ^2 direction with $C_2 = 0.3$ with coefficients of gradient and curvature $\alpha = 1, \beta = 1$, respectively.

double wedge (supersonic Euler)

Results obtained from a supersonic flow at Mach = 2 over fine (121 x 41) and coarse (81 x 31) double–wedge grids are shown in Figures 3–7. Figure 3 shows the pressure contours obtained from 300 time steps on the initial and adaptive grids (121 x 41). The grid was adapted to the density gradient in the flow direction (RHO = 1,0) with $C_1 = 0.7$ and to the pressure gradient in the normal direction with $C_2 = 0.5$. A total of 4 adaptations was used for this case, with control functions updated from the previous grid.

Figure 4 shows the pressure coefficients on the lower wall, and convergence histories of the two solutions are shown in Figure 5. In Figure 5, the high peaks at each adaptation are due to the use of the previous solution on the new adapted grid without integration onto the new grid. From these figures, clearly the adaptive grid gives a much better representation of the shock regions as well as the expansion regions. Shocks are much sharper for the solution obtained on the adaptive grid. A record of the CPU time on an IRIS 4D/440VGX machine shows that the total CPU time for the initial grid (121 x 41) without adaptation was 1481.51 CPU seconds and for the adaptive grid (121 x 41) was 1599.02 CPU seconds, an 8% increase.

Contour plots on the pressure of the initial fine grid (121 x 41), the initial coarse grid (81 x 31), and the adaptive grid (81 x 31) are shown in Figure 6. The coarse grid was adapted to the combination of density and pressure in ξ^1 direction, with weight coefficient $C_1 = 0.5$, and to the gradient of this combination in ξ^2 direction with weight coefficient $C_2 = 0.5$, ($AWT = VAR, GRAD, RHO$ = 1,1, $PRES$ = 1,1).

Different adaptive mechanisms applied to the coarse grid in the multiple adaptation process are shown in Figure 7. Figure 7b shows the pressure contours obtained on the adaptive grid of Figure 7a. The initial grid was adapted to the curvature of the combination of density and pressure in both directions ($AWT = CURV, CURV, RHO$ = 1,1, $PRES$ = 1,1). The total number of adaptations was 4 with $C_1 = 0.7$, $C_2 = 0.7$. The coefficients of the gradient and curvature were $\alpha = 1$ and $\beta = 0.5$, respectively, and the updates were from the original control functions.

Figure 7d shows the pressure contours obtained on the adaptive grid of Figure 7c. The adaptative mechanism for this case was pressure gradient in both directions with $C_1 = 0.7$, $C_2 = 0.7$ and total number of adaptations was 4, ($AWT = GRAD, GRAD, RHO$ = 0,0, $PRES$ = 1,1).

The initial grid, adapted to the gradient of the combination of density and pressure in the ξ^2 direction only is shown in Figure 7e. Total number of adaptations was 5 with $C_1 = 0$, $C_2 = 0.9$, and updates were applied to the previous control functions. Pressure contours obtained from this adaptive grid are shown in Figure 7f.

From these figures, the representation of the shocks on the adapted coarse grid is much sharper and closer to the fine grid solution than the nonadaptive coarse grid. The total CPU time for obtaining 300 time steps solution for the adaptive grid was approximately 800 seconds for each adaptive mechanism, nearly 50% saving time compared to that of the fine grid.

The adaptation to the combination of density and pressure in ξ^1 direction and to the gradient of this combination in ξ^2 direction of Figure 6 gives a smoother behavior of the pressure coefficient behind the shock than the adaptation to the gradient of pressure alone of Figures 7c and 7d. The adaptation to the curvature of Figures 7a and 7b gives a better result, however with a little over prediction of the pressure coefficient right behind the shock. The adaptation to the gradient of the combination of the density and pressure in ξ^2 direction only in Figures 7e and 7f gives the closest solution to the fine grid solution.

From these results, clearly multiple adaptive grids produce a better representation of the shock regions, as well as the expansion regions, than that of the same nonadaptive grid. Among these adaptive mechanisms, the use of the better results than the use of single variable. Another advantage that should be mentioned here is the controlling of the direction in which adaptation is applied. As shown above, the adaptation in only one direction (ξ^2) gives the closest solution to the fine grid solution. Moreover, the grid in this adaptive mechanism is not being disturbed as much as by the adaptation in both directions. The minimum skew angle for this case is higher compared to those of adaptation in both directions. Of course, this is true only for a certain number of adaptations and a particular value of weight coefficients.

wind tunnel (supersonic Euler)

Results from the supersonic flow at Mach = 2 in a wind tunnel are shown in Figure 8. These results were also obtained in 300 time steps. Figure 8a is the initial grid, Figure 8b is the adaptive grid adapted to the error estimation in both directions, and Figure 8c is the adaptive grid adapted to gradient of the combination of density and pressure in both directions. The number of adaptations was 5 for both cases, with $C_1 = 0.6$, $C_2 = 0.55$ for the adaptation to gradient of the combination. Shocks are much sharper for solutions obtained on the adaptive grids than on the nonadaptive grids for this configuration in supersonic flow as well.

Results from these examples show that multiple adaptive grids captured very well major features of the flow field in supersonic flow for these particular configurations. The adaptations to the combination of the grid quality measures, such as skewness of the grid and the flow solution, for these particular grids not only make the grid more skewed but also resulted in poor resolution of the major features of the flow field. On the other hand the adaptation to the error estimation and the use of the weighted average in weight functions computed from several flow variables does, in fact, improve the solutions.

The computation of the weight functions and the choice of the adaptive solution variable are independent from one direction to another thus enabling the users to have more freedom in choosing suitable adaptive mechanism for each kind of flow. For example, in the case of boundary layers and shocks occurring in the same flow field, the users may choose to adapt the grid to the velocity magnitude gradient in the normal direction to capture the boundary layer regions and to the pressure gradient in the flow direction to capture the shocks.

backward facing step (incompressible Navier–Stokes)

Results of multiple adaptation performed with the adaptive INS3D incompressible flow code are shown in Figures 9–12. These results are obtained for incompressible laminar flow for a

2−block backward facing step, (grid size for the first block is (21 x 35) and (81 x 41) for the second block). The Reynolds number used in this investigation for the backward facing step was 183.32 for comparison with experimental data.

The grid constructed for the backward facing step considered in this case is the same as the geometry of the experiment. However, the step length downstream of the grid is only 30 times the length of the step height, while the step length for the experiment was much larger. Figure 9c shows the velocity magnitude contours obtained from 5000 time steps on the initial grid of Figure 9a. Velocity vectors are shown in Figure 9b.. Figure 10 shows the velocity magnitude, vorticity contours and velocity vectors obtained from 5000 time steps on the adaptive grid. The initial grid was adapted at 500 and 1000 time steps to the vorticity magnitude in the direction normal to the walls with $C_1 = 0$, $C_2 = 1$, (*AWT = VAR, VAR, VORR* = 0,1). Total number of adaptations was 2 for this case, and updates were applied to the initial control functions.

Skin friction coefficients on the lower and upper walls (beginning at the step) obtained from initial and adaptive grids are plotted in Figure 11. Velocity profiles at the step and several locations downstream (nearest to the experimental data) along with digitized experimental data are shown in Figure 12.

Results from these figures show that the velocity profiles obtained from the adaptive grid are closer to the experimental data than for the nonadaptive grid. However, there are some wiggles of the skin friction coefficient obtained from the adaptive grid occurring at the separation region of the lower wall. This may be due to the redistribution of grid spacings in this region. Digitized values of the reattachment length from Figure 11 are approximately 7.67 for both solutions, while the experimental value was 7.9 for this particular Reynolds number. The difference of these values may be due to the difference of the step length of the experiment and the grid downstream.

A record of the CPU time on a Cray 2 machine shows that the total CPU time for the initial grid without adaptation was 25956.26 CPU seconds and for the adaptive grid was 26363.74 CPU seconds. Since there is only 2 adaptive iterations the increase in time for this case is 1.2%.

180 degree turn around duct (incompressible Navier–Stokes)

Most flow solvers for incompressible flow require grid lines which are packed closely to the walls in order to resolve the boundary layer regions. This results in a large number of grid points and hence long computer times. The multiple adaptation can be used to reduce the cost of computer time by allowing the use of a coarser grid. In the present investigation, a fine grid (111 x 51) with spacing off the walls of 0.002 and a coarse grid (111 x 31) with spacing 0.004 off the walls are considered for the turn around duct. The result of the adaptation on the coarse grid is compared with the nonadaptive fine grid solution, while the Reynolds number for the turn around duct was 500. Results obtained from 6000 time steps on fine, coarse and adaptive grids for turn around duct are shown in Figures 9−18.

Figure 13 shows the velocity magnitude contours obtained on the initial and adaptive grids. The initial coarse grid was adapted to the velocity magnitude gradient at 1000, 1500, 2000 and 2500 time steps, in the direction normal to the flow direction, (*AWT = GRAD, GRAD, VOMA* = 0,1). Total number of adaptations was 4 with $C_1 = 0.1$, $C_2 = 0.5$, and the updates were applied to the initial control functions. Figures 14 and 15 show the skin friction and pressure coefficients of the inner and outer walls obtained from coarse, fine and adaptive coarse grids.

Figure 14 shows that the behavior of the skin friction coefficients for the adaptive grid are much closer to the fine grid solution than the nonadaptive coarse grid. Figure 15 shows that the adaptation for this case did not help significantly in the improvement of the pressure coefficients, however.

Figure 16 shows the velocity magnitude contours obtained on the initial and another adaptive grid. The initial coarse grid was adapted to the combination of vorticity and quality measure aspect ratio of the grid in the direction normal to the flow direction, (*AWT = VAR, VAR, VORR* = 0,1, *ASPE* = 1). Here $C_1 = 0.3$, $C_2 = 0.5$. Figures 17 and 18 show the skin friction and pressure coefficients of the inner and outer walls obtained from coarse, fine and adaptive coarse grids.

Figure 17 shows that the behavior of the skin friction coefficient of the outer wall is almost identical to that of the fine grid. The representation of the skin friction of the inner wall is smoother than that of the nonadaptive grid but with a large change after the separation region toward the outlet of the duct. Figure 18, again indicates that the adaptation did not help in the improvement of the pressure coefficients for this case either.

A record of the CPU time on an IRIS 4D/440VGX machine shows that the total CPU time for the initial grid (111 x 51) was 23870.61 CPU seconds and for the adaptive grid (111 x 31) was approximately 13800 CPU seconds for each adaptive mechanism. From Figures 13 and 16, it can be seen that in both adaptations the grids get finer at the turn. Correspondingly the skin friction coefficients obtained from adaptive grids have higher pick at the turn and capture separation region well, as shown in Figures 14 and 17. Moreover, the reattachment point obtained from adaptive grid of Figure 14 is closer to that of the fine grid than the adaptation of Figure 17 and the non−adaptive grid.

CONCLUSIONS

The widely−used EAGLE grid generation system (Ref. 14) has been extended and enhanced so that it can be readily coupled with existing PDE solvers which operate on structured grids to provide a flexible adaptive grid capability. The adaptive EAGLE grid code can be used for generating not only algebraic grids and elliptic grids but static adaptive grids as well. In the static adaptation, the grid can be adapted to an existing PDE solution or to grid quality measures or to a combination of both. The test cases show that some grid properties can be improved by the static adaptation to grid quality measures.

In this study, the weight functions can be formulated as weighted average of weight functions from several flow variables or several quality measures or the combination of both. Different weight functions and adaptive variables can be applied in each direction. These operations are controlled through the input parameters in static as well as multiple adaptation mode.

There are several successful incorporations of the adaptive EAGLE packed subroutines into flow codes, including INS3D from NASA Ames and the MISSE Euler solver developed at Mississippi State University. Several configurations are considered for each of these adaptive flow codes for the investigation of the new weight functions formulations and grid quality measures in the multiple adaptation.

Results obtained from the adaptive MISSE Euler flow code show considerable success as measured by improvements in shock resolution on coarse grids in the compressible flows. Some success has been made in capturing separation regions on coarse grids of the adaptive INS3D flow code in incompressible flows. For further study, the interpolation of the previous solutions to the new adapted grids would be recommended, especially for the adaptive INS3D flow code and the implementation of arbitrary block adaptation in multi−block configurations.

ACKNOWLEDGEMENT

This work was supported in part by Grant F08635−89−C−0209 from the Air Force Armament Directorate, Eglin AFB, (Dr. Lawrence Lijewski, monitor) and in part by Contract NAS8−36949 from NASA Marshall Space Flight Center (Dr. Paul McConnaughey, monitor).

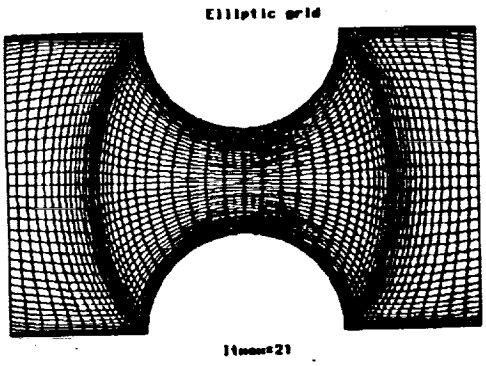

Figure 1a. Elliptic Grid

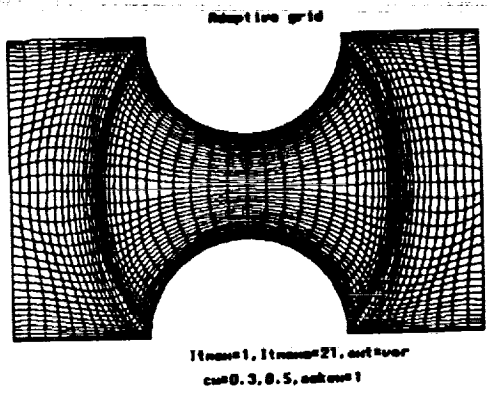

Figure 1b. Adaptation to skewness.

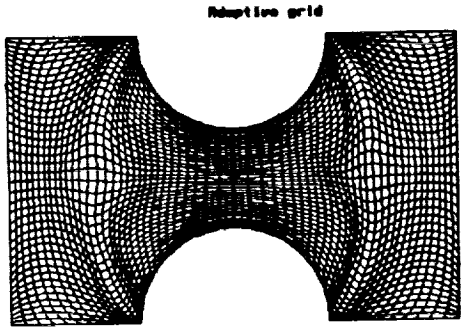

Figure 1c. Adaptation to aspect ratio.

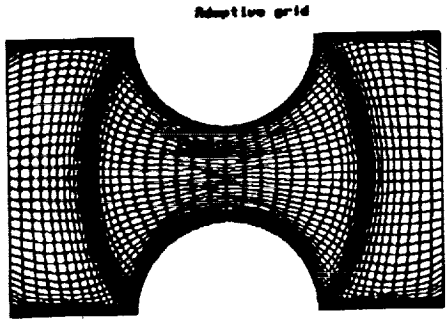

Figure 1d. Adaptation to Laplacian.

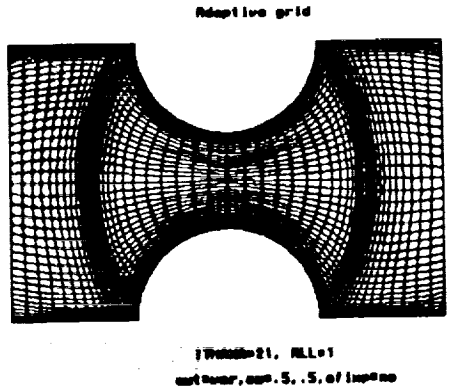

Figure 1e. Adaptation to skewness, aspect ratio, and Laplacian.

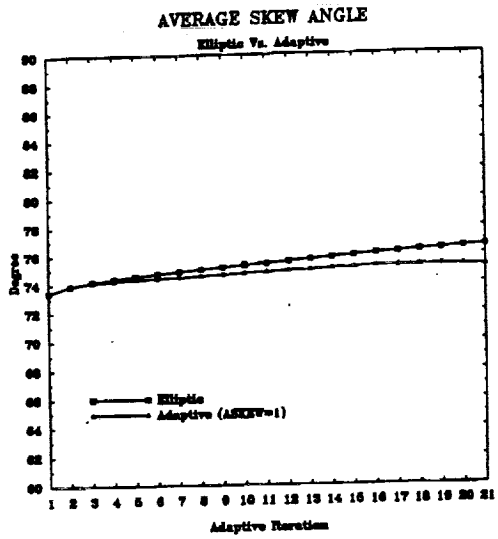

Figure 2a. The difference of average skew angle between initial and adaptive grids.

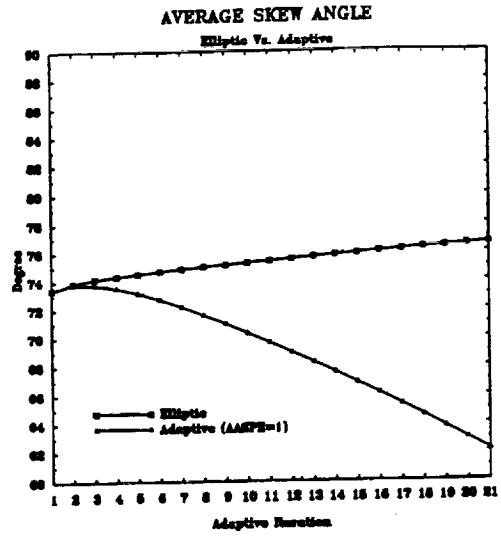

Figure 2b. The decreasing of average skew angle in the adaptation to aspect ratio.

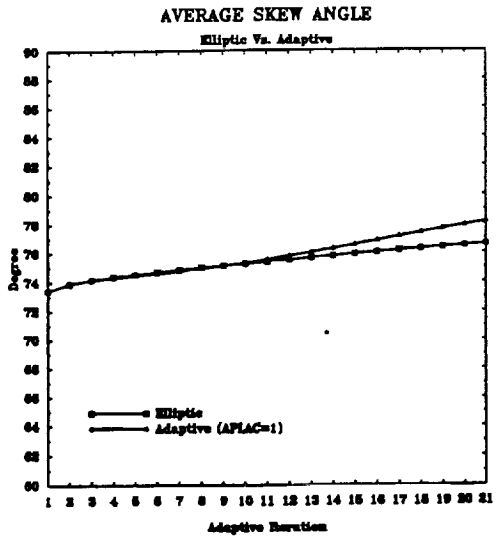

Figure 2c. The increasing of average skew angle in the adaptation to Laplacian of the grid.

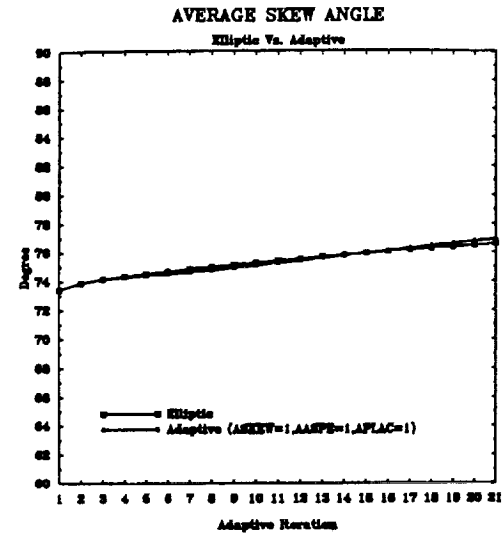

Figure 2d. Average skew angle in the adaptation to all grid quality measures.

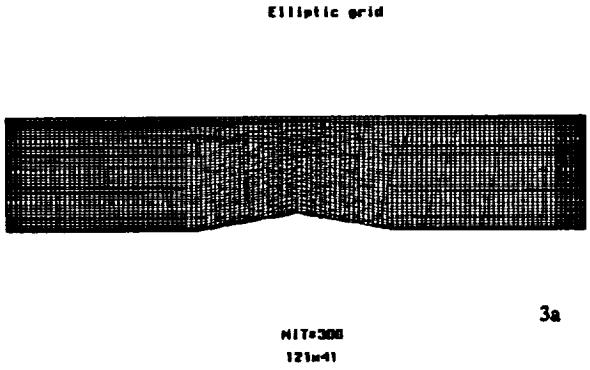

3a

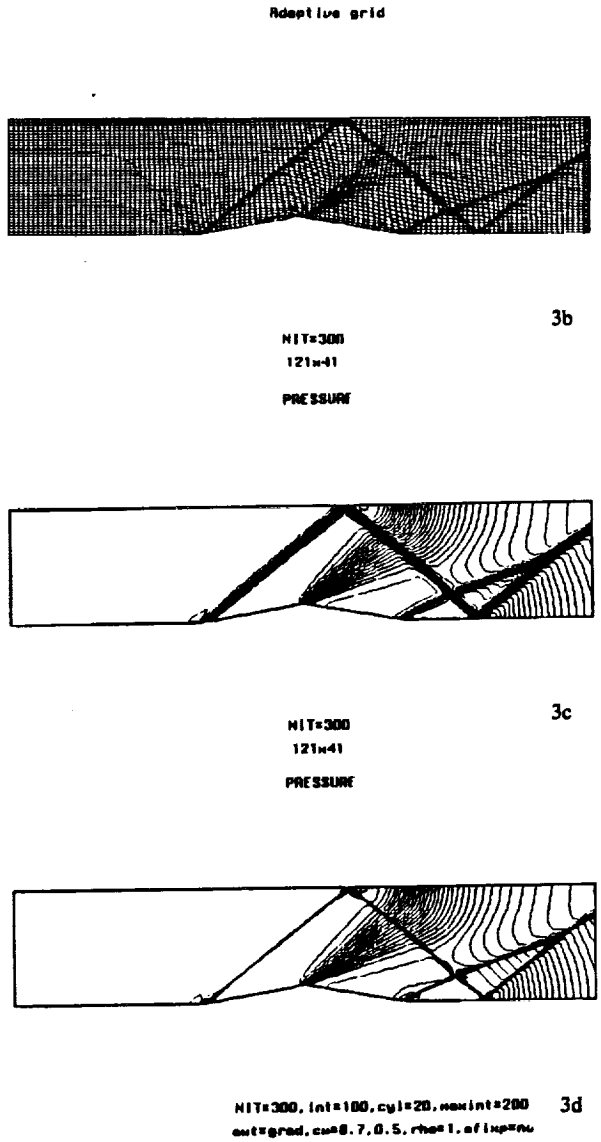

3b

3c

3d

Figure 3. Contour plots of pressure on initial and adaptive grids.

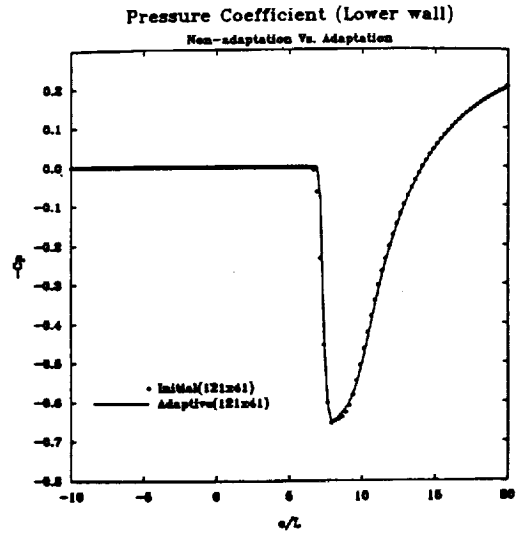

Figure 4. Adaptation with *awt* = *grad, grad, PRES* = 1,1, *cw* = 0.7, 0.7.

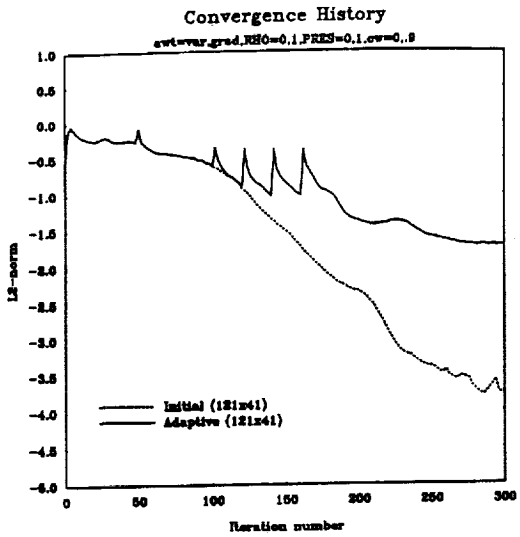

Figure 5. Convergence history of the initial and adaptive grid solutions.

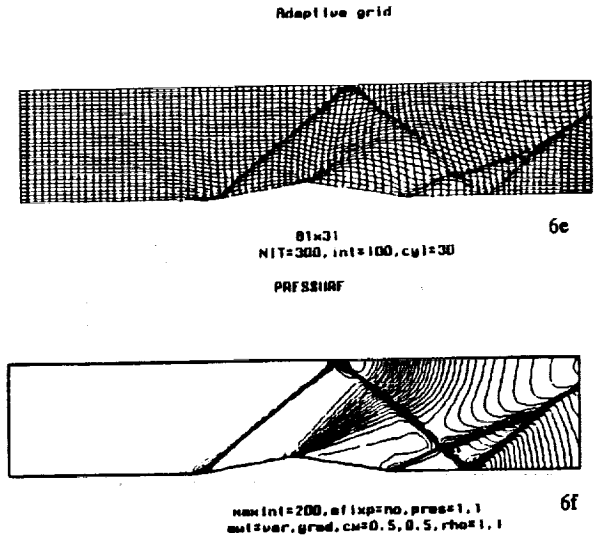

Figure 6. Contour plots of the pressure on fine, coarse and adaptive grids.

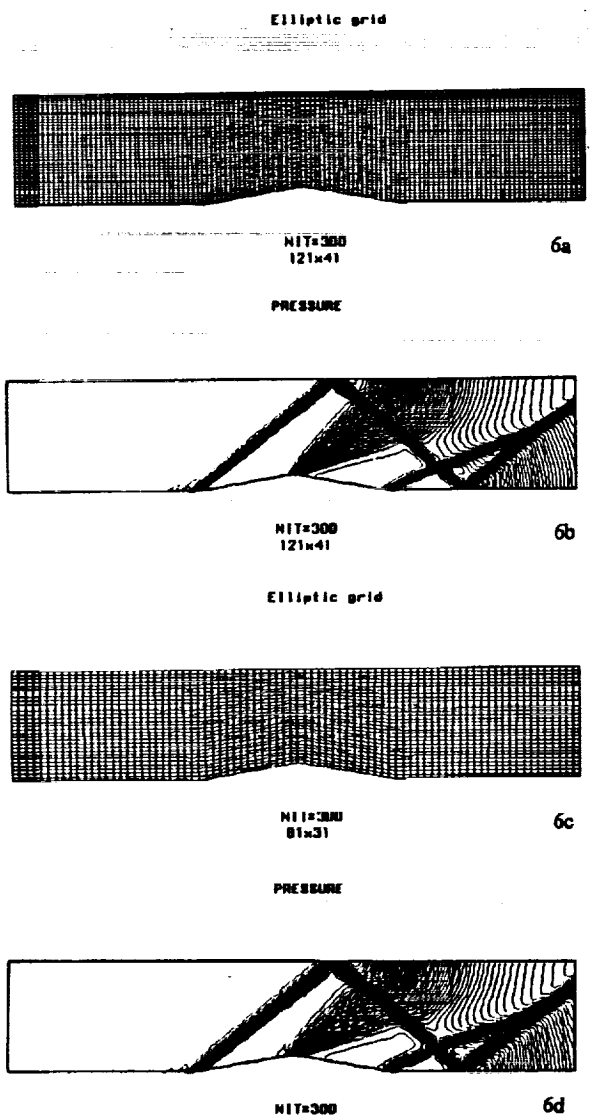

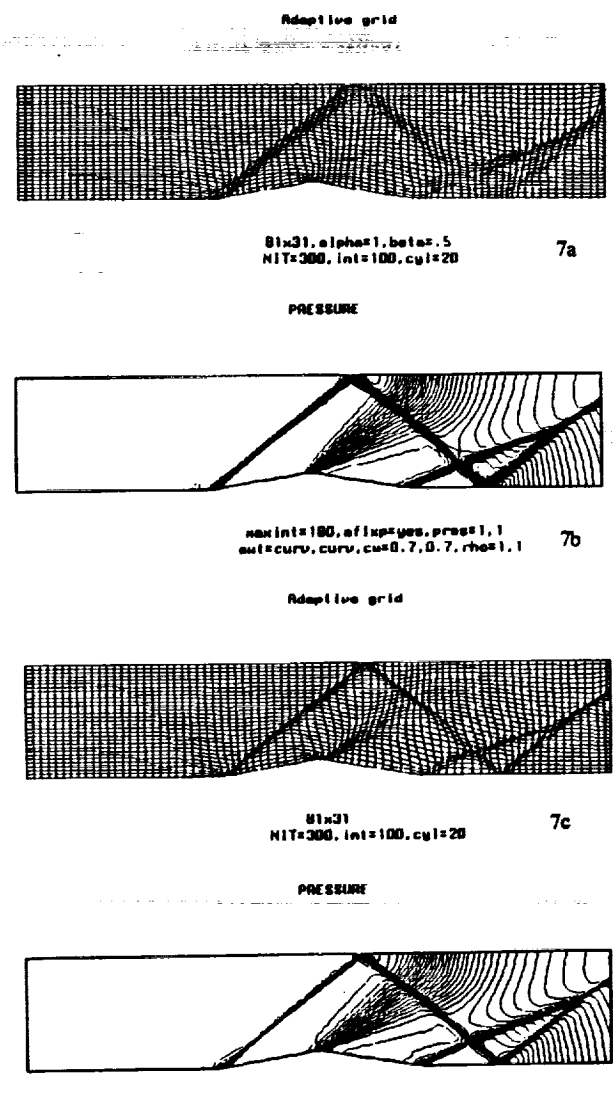

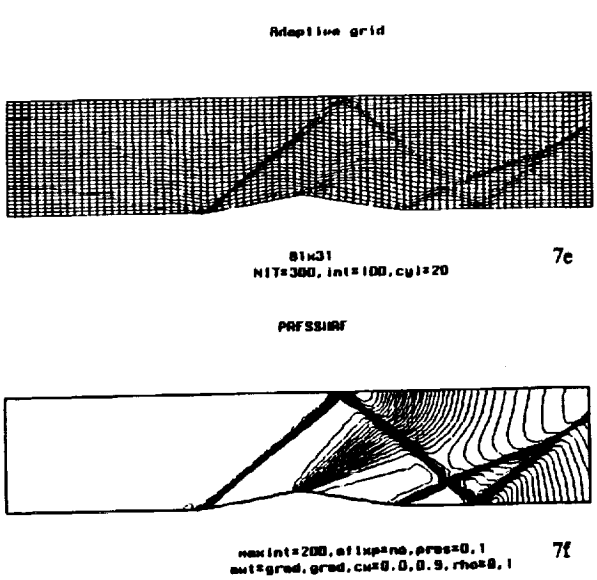

Figure 7. Contour plots of pressure on adaptive grids.

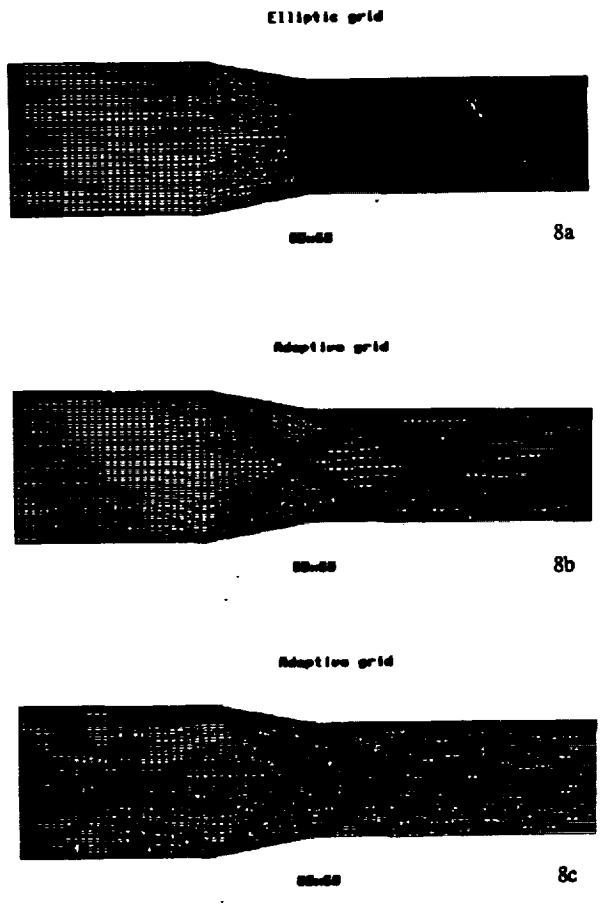

Figure 8. Contour plots of pressure on initial and adaptive grids.

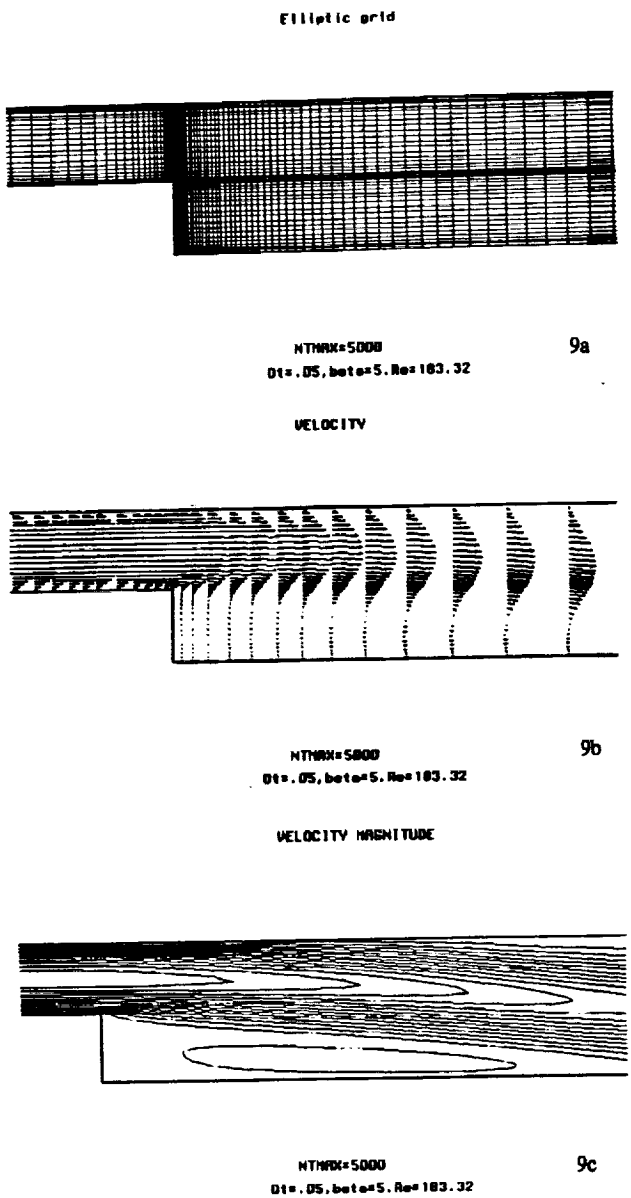

Figure 9. Contour plots of velocity magnitude, and velocity vectors on initial grids.

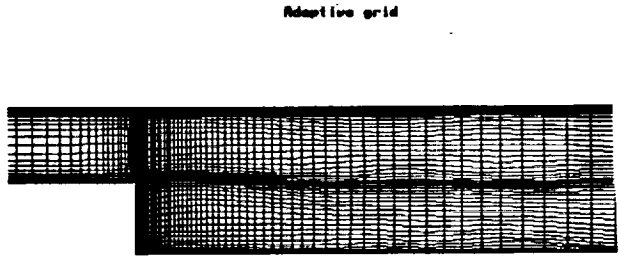

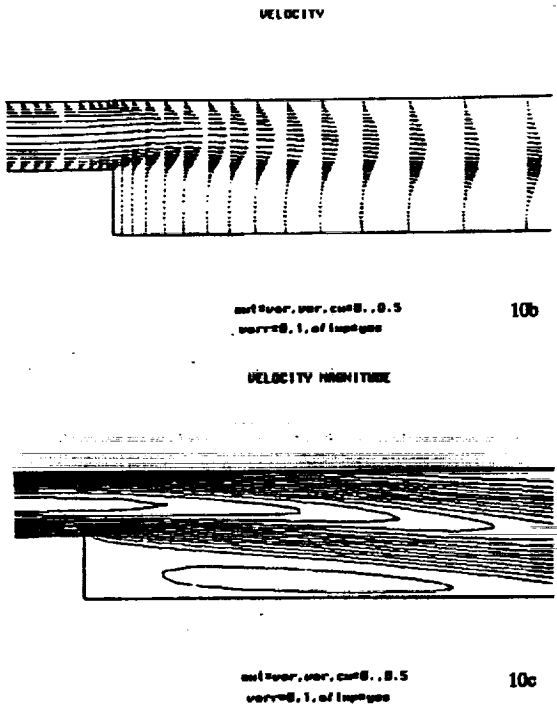

Figure 10. Contour plots of velocity magnitude and velocity vectors on adaptive grid.

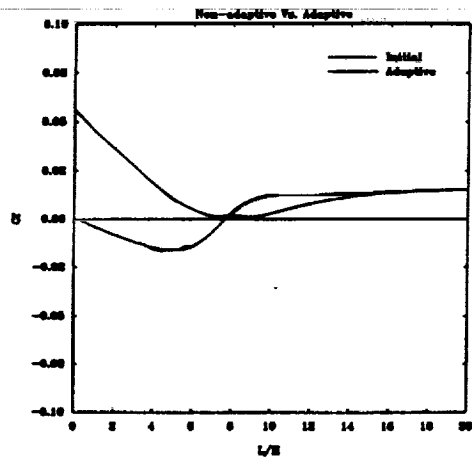

Figure 11. Skin friction of the lower and upper walls obtained from initial and adaptive grids.

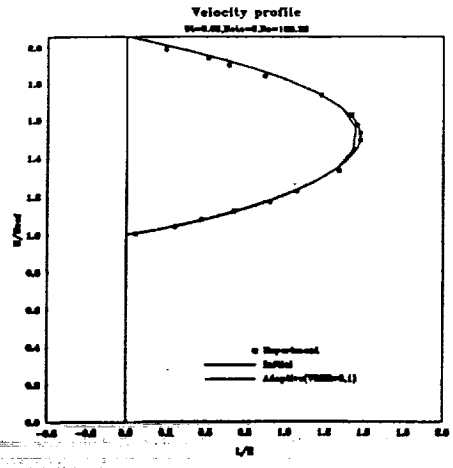

12a

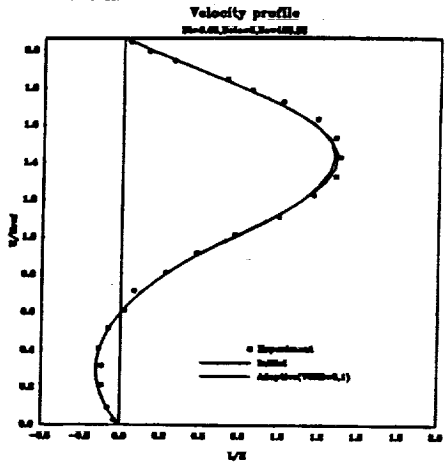

12b

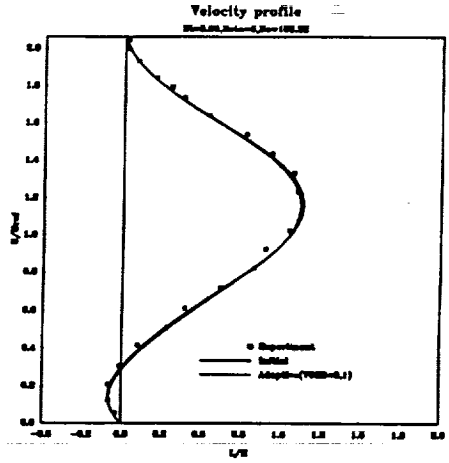

12c

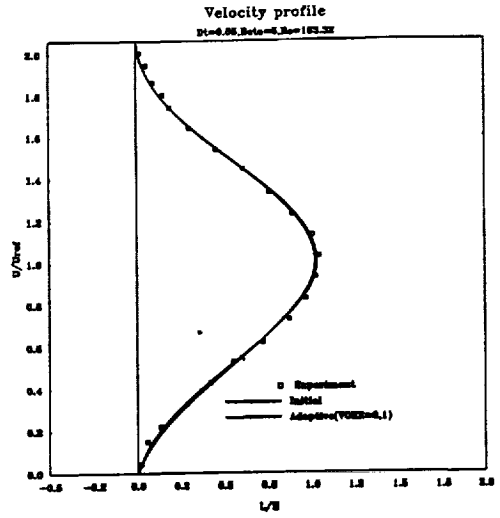

12d

Figure 12. Velocity profile at the step $x = 2.77, x = 6.27$, and $x = 8.128$.

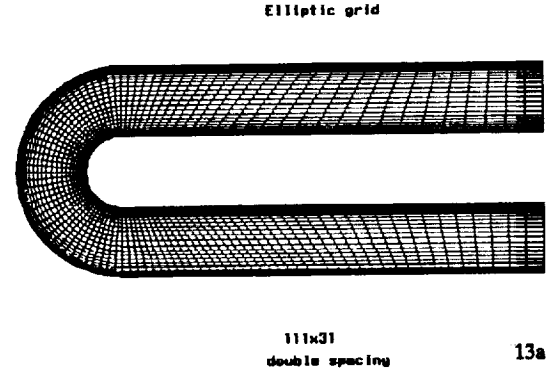

13a

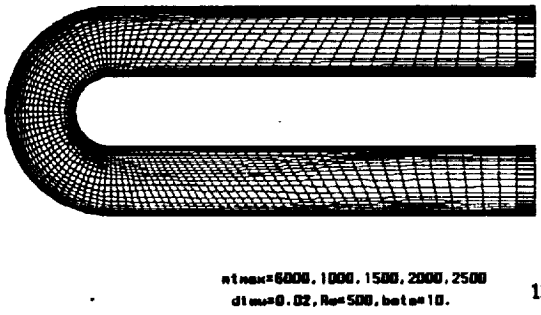

13b

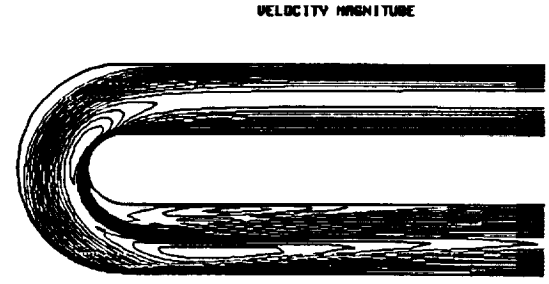

13c

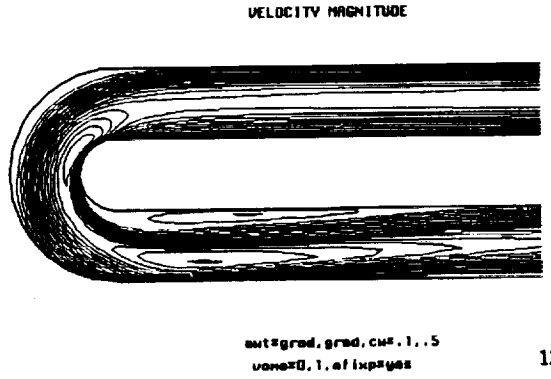

13d

Figure 13. Contour plots of velocity magnitude on initial coarse grid and adaptive coarse grid with *awt* = *grad, grad, VOMA* = 0,1, *cw* = 0.1, 0.5.

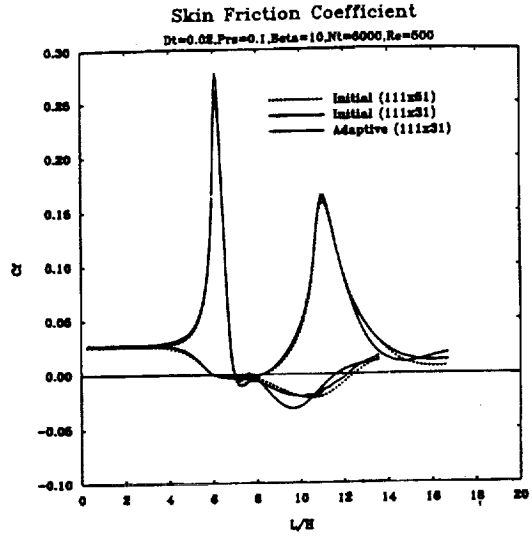

Figure 14. Skin friction coefficients of the inner and outer walls obtained from initial fine, coarse and adaptive grids with *awt* = *grad, grad, VOMA* = 0,1, *cw* = 0.1, 0.5.

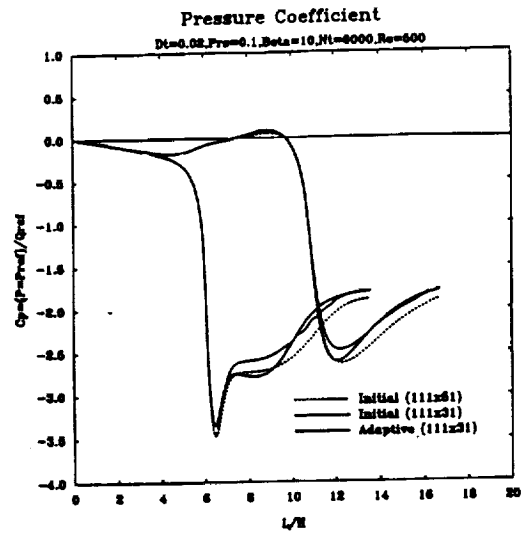

Figure 15. Pressure coefficients of the inner and outer walls obtained from initial fine, coarse and adaptive coarse grids with *awt* = *grad, grad, VOMA* = 0,1, *cw* = 0.1, 0.5.

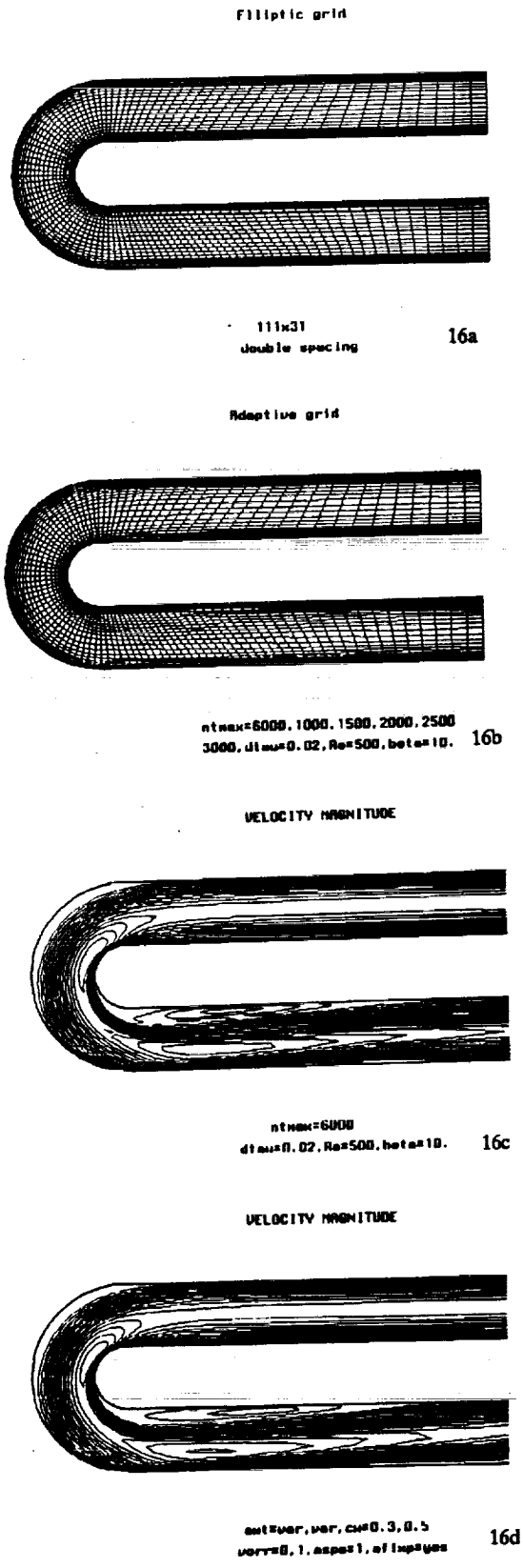

Figure 16. Contour plots of velocity magnitude on initial coarse grid and adaptive coarse grid with *awt* = *var, var, VORR* = 0,1, *ASPE* = 1, *cw* = 0.1, 0.5.

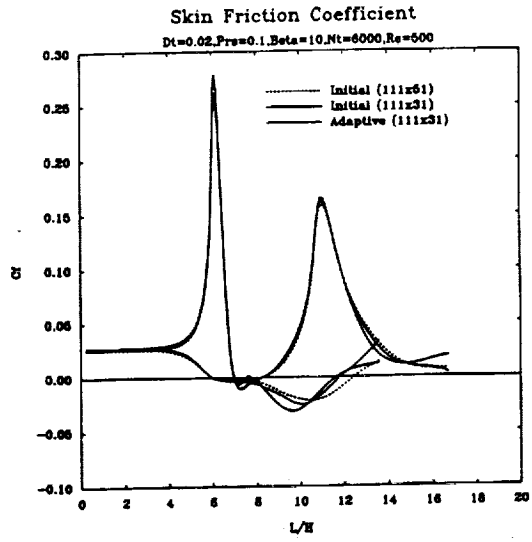

Figure 17. Skin friction coefficients of the inner and outer walls obtained from initial fine, coarse and adaptive coarse grids with *awt* = *var, var, VORR* = 0,1, *ASPE* = 1, *cw* = 0.1, 0.5.

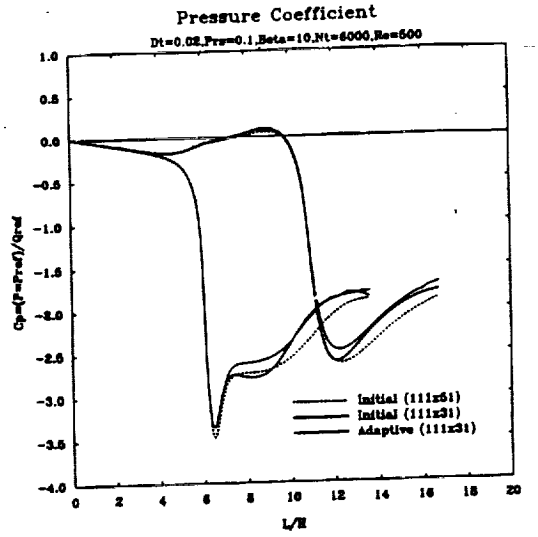

Figure 18. Pressure coefficients of the inner and outer walls obtained from initial fine, coarse and adaptive coarse grids with *awt* = *var, var, VORR* = 0,1, *ASPE* = 1, *cw* = 0.1, 0.5.

REFERENCES

1. J. F. Thompson "A Survey of Dynamically–Adaptive Grids in the Numerical Solution of PDE", *Journal of Applied Numerical Mathematics*, Vol. 1, pp. 3–27, North–Holland, 1985.
2. H. J. Kim and J. F. Thompson, "Three Dimensional Adaptive Grid Generation on a Composite Block Grid", *AIAA* 88–0311, *AIAA* 26th Aerospace Sciences Meeting, Reno, Nevada, 1988.
3. J. Tu and J. F. Thompson, "Three Dimensional Solution–Adaptive Grid Generation on Composite Configurations", *AIAA* 90–0329, *AIAA* 28th Aerospace Sciences Meeting, Reno, Nevada, 1990.
4. D. A. Anderson, "Equidistribution Schemes, Poisson Generators, and Adaptive Grids", *Applied Mathematics and Computation*, Vol. 24, p. 211, 1987.
5. D. A. Anderson, "Generating Adaptive Grids with Conventional Grid Scheme", *AIAA* 86–0427, *AIAA* 24th Aerospace Science Meeting, Reno, Nevada, 1986.
6. B. F. Johnson and J. F. Thompson, "Discussion of a Depth–Dependant Adaptive Grid Generator for Use in Computational Hydraulics", *Numerical Grid Generation in Computational Fluid Mechanics*, J. Hauser and C. Taylor, Ed., Pineridge Press, 1986.
7. P. R. Eiseman, "Adaptive Grid Generation", *Computer Methods in Applied Mechanics and Engineering*, Vol. 64, p. 321, 1987.
8. G. D. Kerlick and G. H. Klopfer, "Assessing the Quality of Curvilinear Coordinate Meshes by Decomposing the Jacobian Matrix", *Numerical Grid Generation*, J. F. Thompson, Ed., pp. 787–796, North–Holland, 1982.
9. B. Gatlin, et al., "Extensions to the EAGLE Grid Code for Quality Control and Efficiency", *AIAA* 90–0148, *AIAA* 29th Aerospace Sciences Meeting, Reno, Nevada, 1991.
10. C. W. Mastin, "Error Estimates and Adaptive Grids for the Numerical Solution of Conservation Laws", *Proceedings of the First International Conference on Computation Physics*, pp. 73–76, Boulder, CO, June, 1990.
11. Phu Luong, "Analysis and Control of Grid Quality in Computational Simulation", PhD Dissertation, Mississippi State University, December, 1991.
12. D. L. Whitfield, "Implicit Upwind Finite Volume Scheme for the 3D Euler Equations", Mississippi State University, MSSU–EIRS–ASE–85–1, September, 1985.
13. S. E. Rogers, D. Kwak and J. L. Chang, "INS3D – An Incompressible Navier–Stokes Code in Generalized 3D Coordinates", NASA Technical Memorandum 100012, NASA Ames Research Center, November, 1987.
14. J. F. Thompson, "A Composite Grid Generation Code for General 3D Region – the EAGLE Code", *AIAA Journal*, Vol. 26, No. 3, p. 271, 1988.